

FastCAT: Fast Cone Beam CT (CBCT) Simulation

Jericho O'Connell, Magdalena Bazalova-Carter

University of Victoria, 3800 Finnerty Road, Canada

Version typeset September 8, 2022

Author to whom correspondence should be addressed. email: jerichoo@uvic.ca

Abstract

Purpose: To develop fastCAT, a fast cone-beam computed tomography (CBCT) simulator. The fastCAT application uses pre-calculated Monte Carlo (MC) CBCT scatter and detector response functions to reduce simulation time for kV and MV CBCT.

Methods: Pre-calculated x-ray beam energy spectra, detector optical spread functions and energy deposition, and phantom scatter kernels are combined with beam filtration and GPU raytracing to produce CBCT volumes. Source spectra are either simulated in EGSnrc using 2.5 and 6 MeV electron beams incident on a variety of target materials or analytical spectra from a tungsten x-ray tube. Detectors were modelled in Geant4 extended by Topas including optical transport in the scintillators. Two MV detectors were modelled, a standard Varian AS1200 GOS detector and a novel CWO high quantum efficiency detector. Energy dependent scatter kernels were created in Topas for a two 16-cm diameter water phantoms: a Catphan 515 contrast phantom and a spatial resolution phantom. The Catphan phantom contained inserts of 1-5 mm in diameter of six different tissue types; brain, deflated lung, compact and cortical bone, adipose and B-100. These pre-calculated MC datasets allow the user to create CT volumes with custom phantom inserts, imaging beam, focal spots and detector combinations.

Results: FastCAT simulations retain high fidelity to measurements and MC simulations: MTF curves were within 1.1% and 4.8% of measured values for the CWO and GOS detectors, respectively. Contrast in a fastCAT Catphan 515 simulation was seen to be within 1% of an equivalent MC simulation for all of the tissues. A fastCAT simulation of the Catphan 515 module at a resolution of $1024 \times 1024 \times 10$ took 61 seconds on a GPU while the equivalent Topas MC was estimated to take approximately 5.6 CPU years.

Conclusions: We present an open source fast CBCT simulation with high fidelity to MC simulations. The fastCAT application can be found at <https://github.com/jerichoconnell/fastCAT.git>.

Contents

I. Introduction	1
II. Materials and Methods	2
II.A. Imaging Beam	2
II.B. Detector Simulation	4
II.C. Imaging Phantom	5
II.D. Scatter Correction	5
II.E. Raytracing	6
II.F. Noise and CBCT reconstruction	7
II.G. Dose calculation	8
III. Results	9
III.A. Detector MTF	9
III.B. Projections and dose	9
III.C. CBCT contrast and calculation time	11
IV. Discussion	12
IV.A. Limitations	12
IV.B. Future applications	14
V. Conclusion	15
VI. Acknowledgments	15
References	15

I. Introduction

Cone beam computed tomography (CBCT) is applied extensively in clinical radiotherapy, CBCT enables image-guided radiotherapy (IGRT) for the verification of patient positioning¹, quality assurance of treatment plans^{2,3}, and real time tumor localization¹. Two different methods of CBCT are clinically applied, both of which include a source and detector mounted on a rotating gantry. The most common CBCT system uses a gantry mounted kilovoltage (kV) x-ray source. Which is known as on-board imaging or kV-CBCT imaging. Detectors in kV-CBCT can be thin and made of low Z materials since the beams are not very penetrating. Conversely, a megavoltage (MV) treatment beam can be used as the source in MV-CBCT imaging. MV detectors, also know as electronic portal imaging devices (EPIDs), are generally made of higher Z materials and are thicker to stop high energy x-rays. kV-CBCT is has better soft tissue contrast and higher image quality than MV-CBCT⁴. However, kV-CBCT requires an additional source and detector. Conversely, MV-CBCT generally has reduced image quality and is used in specific applications such as high-Z material artifact suppression^{5,6} but does not require an additional source. Performance of these imaging modalities is dependent on the source spectrum and detector design. As such, EPID development and imaging beam optimization are active areas of research. To optimize new imaging techniques Monte Carlo (MC) simulation methods are often used. These techniques enable the evaluation of imaging setups without creating an expensive prototype of the detector or source.

These MC EPID simulations are accurate but exceptionally computationally demanding since a large number of particles need to be simulated to form the image. The long simulation time can be primarily attributed to two factors. Firstly, MV detectors generally have low detector quantum efficiency (DQE), meaning that many particles that are transported in the simulation do not interact with the detector and do not form an image; a typical EPID DQE may be as low as 1%-1.5%^{7,8}. Secondly, the scintillator in which the optical photons are produced have a high scintillation yield; generating thousands of optical photons per interaction event. These two factors combined result in simulation times often as long as 3000 CPU hours for a 10^7 primary x-ray simulation⁹. Further, to produce a clinically equivalent image of 0.01 MU with a $10 \times 10 \text{cm}^2$ field size one would need more than 10^{11} photons, translating to 3×10^7 CPU hours^{10,11,12}. This problem is compounded in CBCT simulation, where it is necessary to simulate many views of the object for CBCT image

reconstruction.

Large headway has been made to reduce this computational overhead. Star-lack *et al.*¹¹ have shown that one can simulate the detector response with only a fraction of the scintillation yield, significantly reducing the computation time. Likewise, by pre-calculating the optical spread function from the detector and convolving it with the incident particles in the detector the scintillation simulation can be avoided completely^{13,14}. Additionally, Shi *et al.* introduced the fastEPID framework which pre-calculates energy deposition efficiency (η) and optical spread function (OSF) to remove particle transport in the detector entirely without loss of image quality¹⁰. However, these simulations are still seen to be computationally intensive with one image at 1 MU taking 1.540×10^4 CPU hours.

In this work we extend the fastEPID pre-calculation of MC data further by pre-calculating the energy spectrum of the beam source as well as energy dependent scatter kernels for a cylindrical water phantom. We combine this data with an analytical graphical processing unit (GPU) raytracer to provide the primary particle attenuation. We developed fastCAT, a flexible framework for novel beam, beam filtration, detector, and phantom material combinations that shows agreement with MC simulations and run times on the order of 1 GPU-minute.

II. Materials and Methods

The fastCAT simulation GUI is built on top of xpecgen¹⁵, an open source spectrum generator for kV x-ray tubes written in python (version 3.6). Xpecgen has methods for attenuating spectra, calculating half value layers and a python tk GUI which forms the backbone of fastCAT. Default simulation geometry can be seen in Figure 1: A cone beam collimated to 16 cm^2 at isocenter impinges on a 16 cm diameter cylindrical phantom source at source-to-detector distance (SSD) of 1.52 m and source-to-axis distance (SAD) of 1 m.

II.A. Imaging Beam

FastCAT can use kV or MV beams for CBCT image generation. MV spectra were calculated in EGSnrc/BEAMnrc¹⁶ using a variety of target materials (carbon, aluminum, and tungsten) and electron beam energies (2.5, 6 MeV) (Figure 1 inlay). To generate the spectra a mono-

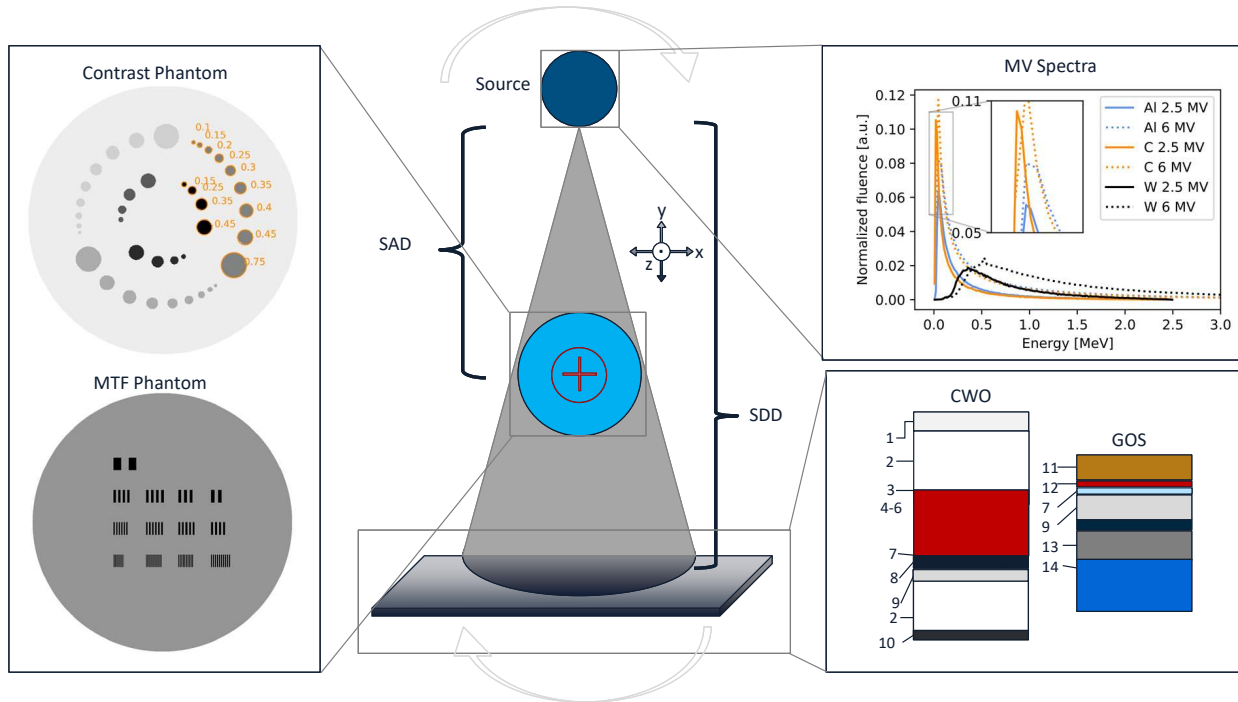


Figure 1: An overview of the simulation setup. Left are the two phantoms used in this work, the Catphan 515 proxy (top) and a modified grid-aligned MTF phantom (bottom). Center is the simulation geometry. To the right is a slice of the GOS (L) and CWO (R) detectors with labels corresponding to Table 2.

energetic electron beam was incident on the target material. The thicknesses of the target materials were based on existing experimental beams for the carbon and aluminum targets¹⁷ and are summarized in Table 1. For the low Z beams (carbon and aluminum) a 2-cm polystyrene filter placed at 50 cm from the target was used to reduce electron fluence in the beam. The photons were collimated by both primary and secondary collimators to create a $10 \times 10 \text{ cm}^2$ field size at and phasespace files were scored at a distance of 100 cm from the target. Energy spectra were generated from the phasespace files for input into fastCAT.

Table 1: Electron target thicknesses used for the generation of the MV imaging beams.

	Tungsten	Aluminum	Carbon
2.5 MV	2.3 mm	6.7 mm ¹⁸	7.6 mm ¹⁹
6 MV	5 mm	8 mm ²⁰	9.9 mm ¹⁹

Table 2: Detector simulation parameters from the work of Shi *et al.*²² and Star-lack *et al.*²¹

	Density (g/cm^3)	Material	Thickness (mm)	Abs. Length Refractive Index	Reflectivity
(1) Carbon Fiber	1.62	C	2.5	–	–
(2) Foam	0.05	C	33.1,25.0	–	–
(3) Vikuiti ESR	1.05	CH	0.065	0.01	0.98
(4) Scintillator Pixel	7.9	CdWO ₄	15	125 2.25	–
(5) Pixel Glue	1.0	Epoxy	15	100 1.47	–
(6) Pixel Septa	2.7	Al Mylar	15	0.001	0.88
(7) Meltmount Glue	1.0	C ₂₁ H ₂₅ ClO ₅	0.01	300 1.7	–
(8) Mylar	1.38	C ₁₀ H ₈ O ₄	0.065	100 1.65	–
(9) AMFPI	2.6	SiO ₂	1	0.001 1.70	–
(10) Fiberglass	1.85	SiO ₂	0.6,6.0	–	–
(11) Copper buildup	8.9	Cu	1	–	–
(12) GOS phosphor	4.59	Gd ₂ O ₂ S:Tb	0.29	43 2.3, 1.0 (binder)	–
(13) Al alloy	2.8	Al	1	–	–
(14) Pb alloy	10.95	Pb	3	–	–

II.B. Detector Simulation

FastCAT currently employs two MV detectors: a novel Cadmium Tungstate²¹ (CWO) detector and a Gadolinium Oxysulfide (GOS) AS1200²² (Varian Medical Systems, Palo Alto, CA) detector. A detector schematic can be seen in Figure 1 while material parameters can be seen in Table 2. The response of the two detectors, including the optical transport, was simulated in Geant4²³ using the Topas²⁴ wrapper. The CWO detector has pixel septa between crystals and has a pixel pitch of 0.784 mm, while the GOS detector has no septa and pixel pitches are set by the active matrix flat-panel imager (AMFPI) pixel pitch. AMFPI pixel pitches of 0.784, 0.392 or 0.336 mm were modelled for the GOS detector and 0.784 and 0.392 mm were modelled for the CWO detector. The detectors were modelled using a modification of the fastEPID framework developed by Shi *et al.*¹⁰. Mono-energetic pencil beams of energies of 30 to 90 keV in 10 keV increments, 100 to 900 keV in 100 keV increments, and 1, 2, 4, and 6 MeV were used to calculate the optical spread function as well as the energy deposition efficiency of each detector. The simulations used the Geant4 Penelope modular toolkit as well as the Geant4 optical physics toolkit with a particle range cut of 5 μm for all particles. To reduce compute time 600 photons per MeV was used as the scintillation yield of both scintillators.

In this work these fastEPID OSF and η were used in two ways. The first way was to generate a detector modulation transfer function (MTF) from the point spread function (PSF): The 2D energy dependent OSFs were weighted by energy deposition efficiency multiplied with the incident spectra from the selected beam to estimate the hypothetical PSF. This PSF was then convolved with an idealized 0.3mm wide slit angled at 2.5 degrees to generate a line spread function (LSF), that was then presampled to estimated the hypothetical MTF. The second use of these parameters was in the fastCAT CT simulation to generate the detector response which is discussed in section II.C.

II.C. Imaging Phantom

Two phantoms can currently be imaged in fastCAT (Figure 1); a pseudo Catphan 515 module (The Phantom Laboratory, Salem NY) and a modified Catphan MTF module with grid aligned rectangular inserts of spatial frequencies between 1 lp/cm to 32 lp/cm. The Catphan 515 phantom contains inserts of 5 to 15-mm in diameter filled with five contrast materials. The default contrast materials in the Catphan 515 phantom are deflated lung, compact and cortical bone, adipose, brain and B-100, with material composition as defined in Geant4 default materials. Thus, for arbitrary phantoms these scatter kernels will not necessarily be valid and should be used with caution. The phantom files are arbitrary voxelized geometries, with slices of up to 1024×1024 voxels in the x-y plane. Phantoms are defined by an array of integer values and a corresponding material map. The defined materials in fastCAT include elements up to Uranium, materials defined in the NIST XCOM database²⁵, and Geant4²³ default materials. Additional materials can be uploaded as a text file containing the energy and linear attenuation coefficient vectors.

II.D. Scatter Correction

The scatter correction for a 16-cm diameter water phantom was generated in Topas using 16 mono-energetic cone beams using the default setup. A phasespace file was collected at the surface of a $40\text{cm} \times 10\text{cm} \times 3\text{mm}$ air slab. The photons were filtered to reject primary particles by removing photons with energy within 0.5 keV of the original beam energy. The spatial distribution of the scattered particles was scored, averaged in the z direction and fitted to a two parameter curve-fit of the form:

$$y = \left(\frac{a}{\sqrt{x^2 + a^2}} \right)^b \quad (1)$$

Where a and b are fitted parameters and x is the off axis distance. This fit was used to insure a symmetric fit, and it resulted in a root mean squared error lower than the symmetric polynomial fit. The resultant energy distribution of the scatter from each mono-energetic cone beam was neglected in the analysis as sufficiently close agreement was seen when approximating the scatter as mono-energetic. These mono-energetic cone beam scatter curves were then combined with analytical projections to form the CT projection data, as will be discussed below.

II.E. Raytracing

The bulk of the computational work of fastCAT CBCT image generation is in the CT raytracing. In this work the TIGRE²⁶ GPU reconstruction package is used for generating the cone beam forward projections. These primary projections, are denoted as “projections”, they are equivalent to the sum of attenuation coefficient along the path of the ray between the source and detector. This is to be distinguished from what we will call the “intensity profiles” which are the hypothetical counts in a given detector pixel. One forward projection is calculated for each CBCT view for each of the 16 energies. These primary projections are converted to intensity profiles using a flood field intensity profile made with the same geometry and number of photons as the scatter corrections ensuring the correct scaling of the scatter. The scatter corrections (both coherent and incoherent) are then added to the primary intensity profiles. These complete intensity profiles, $I(E)$, are then weighted by the fluence $\phi(E)$ and energy deposition efficiency $\eta(E)$ to form the final intensity I_f as

$$I_f = \sum_E \phi(E)\eta(E)I(E) \quad (2)$$

Additional to these incoherent scatter corrections a coherent scatter correction is approximated analytically for the phantom. Two analytical projections of the phantom are taken at each energy: One projection using the linear attenuation coefficient and another using the attenuation coefficient without coherent scatter. These two projections are subtracted to approximate a coherent scatter profile. To reduce computation time only ten slices

in the z direction are simulated in the default phantoms, $512 \times 512 \times 10$ voxels with voxel sizes of 0.31 mm^3 and $1024 \times 1024 \times 10$ voxels with voxel sizes of 0.16 mm^3 for the Catphan 515 and MTF phantom respectively.

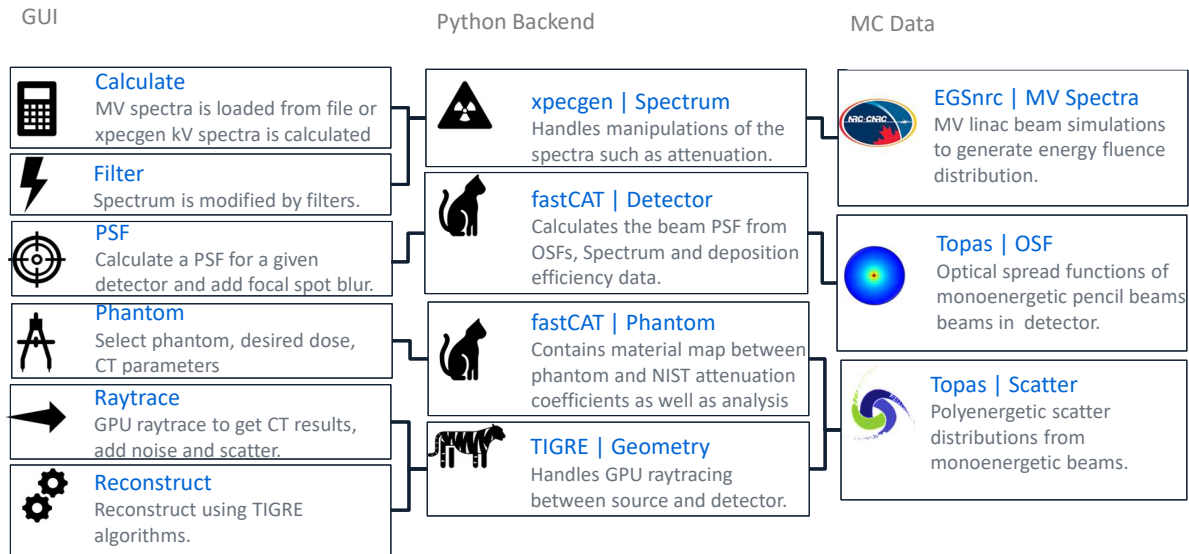


Figure 2: An overview of the parts of the application, on the left are the GUI frames highlighting the user selected parameters. In the center is the backend python objects that hold that execute the analytical functions. On the right are the pre-calculated MC datasets.

II.F. Noise and CBCT reconstruction

Noise is added through an arbitrary Poisson scaling of the intensity profile. This scaling can be related to either dose or particle fluence as will be discussed below. The intensity profiles are then convolved with the OSF at each energy and summed to create a final profile at each angle. These are converted back to projections using the corresponding flood field and are reconstructed. Reconstructions is performed with TIGRE algorithms which have many options for reconstruction types including the default FDK²⁷ and more advanced iterative reconstruction. Image analyses can then be done using specific analysis modules attached to each phantom: For the Catphan 515 module, contrasts and contrast to noise ratios can be calculated while analysis of the MTF phantom gives a measurement of the system MTF.

II.G. Dose calculation

The scaling of the noise in the simulation can be determined by the user based on either the requested dose or particle fluence. Noise defined by particle fluence scales the intensity profile as H ; the total number of particles N_γ divided by the area of the beam A divided by the area of a detector pixel A_p

$$H = \frac{N_\gamma}{A/A_p} \quad (3)$$

Another option is to provide the dose for one view of the phantom. In this case the dose estimate per particle (D_0) at each energy is calculated from:

$$D_0(E) = \frac{1}{N_i} \sum_i E \frac{\mu_{en}(E)}{\mu(E)} (1 - e^{-\mu(E)x_i}), \quad (4)$$

where the index i is summing over each ray in the simulation, μ and μ_{en} are the linear and energy-absorption coefficients respectively, and N_i is the number of rays. These values estimate the average dose per particle at each energy. These doses are weighted by the selected fluence ϕ and summed to get a preliminary total dose estimate D_p per particle

$$D_p = \sum_E \phi(E) D_0(E) \quad (5)$$

These preliminary dose estimates were seen to correlate linearly to doses from MC simulations over all beams ($R^2 > 0.99$). An empirical linear fit is used to relate these estimates to the final dose estimate. The noise is calculated based on the number of particles for the requested dose based on the procedure described above.

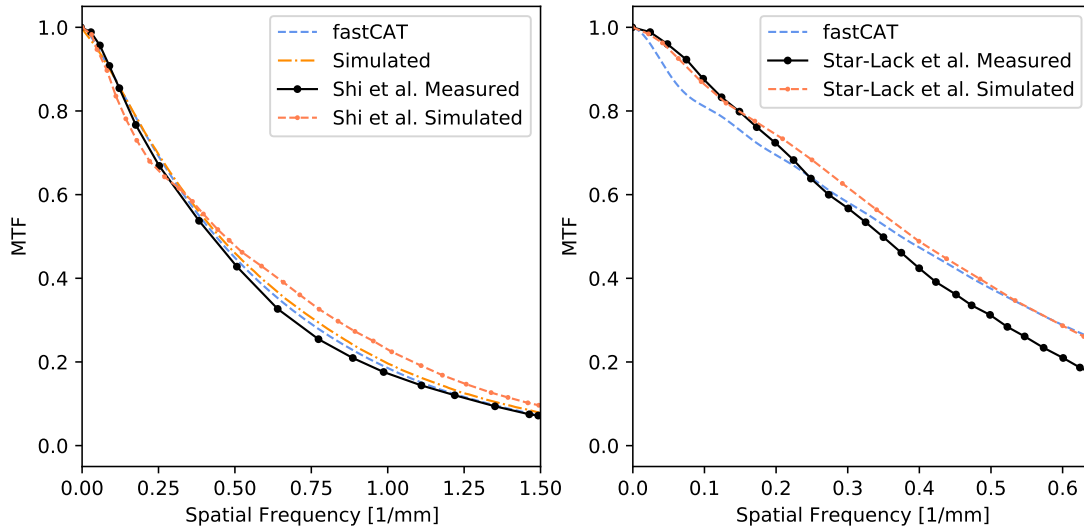


Figure 3: A comparison of fastCAT’s MTF results with measured and simulated values from Shi *et al.* and Star-lack *et al.* respectively.

III. Results

III.A. Detector MTF

FastCAT showed very good agreement with measured and simulated MTFs for both the GOS and CWO detector (Figure 3). For the GOS detector the mean difference between the fastCAT and Topas simulations was 0.5%. The maximum difference was 1.3% at an MTF of 0.32. The mean and maximum difference between the GOS MTF calculated by fastCAT and measurement data provided by Shi *et. al* was 1.1% and 2.6% at an MTF of 0.33. For the CWO detector the mean difference between the fastCAT and the measured data of Star-lack *et al.* was 4.8%. The worst case deviation was 8.4% at an MTF of 0.17.

III.B. Projections and dose

The intensity profiles showed close agreement between fastCAT and Topas (Figure 4 right) exhibiting very little loss in accuracy. The 6 MV aluminum beam had an average deviation of -0.4% between fastCAT and Topas with a worst case accuracy of 1.1%. Likewise, for the Tungsten 6MV beam the fastCAT had an average deviation of -0.2% of the Topas values with a worst case accuracy of 1.4%. The lowest accuracy was likely due to noise in Topas

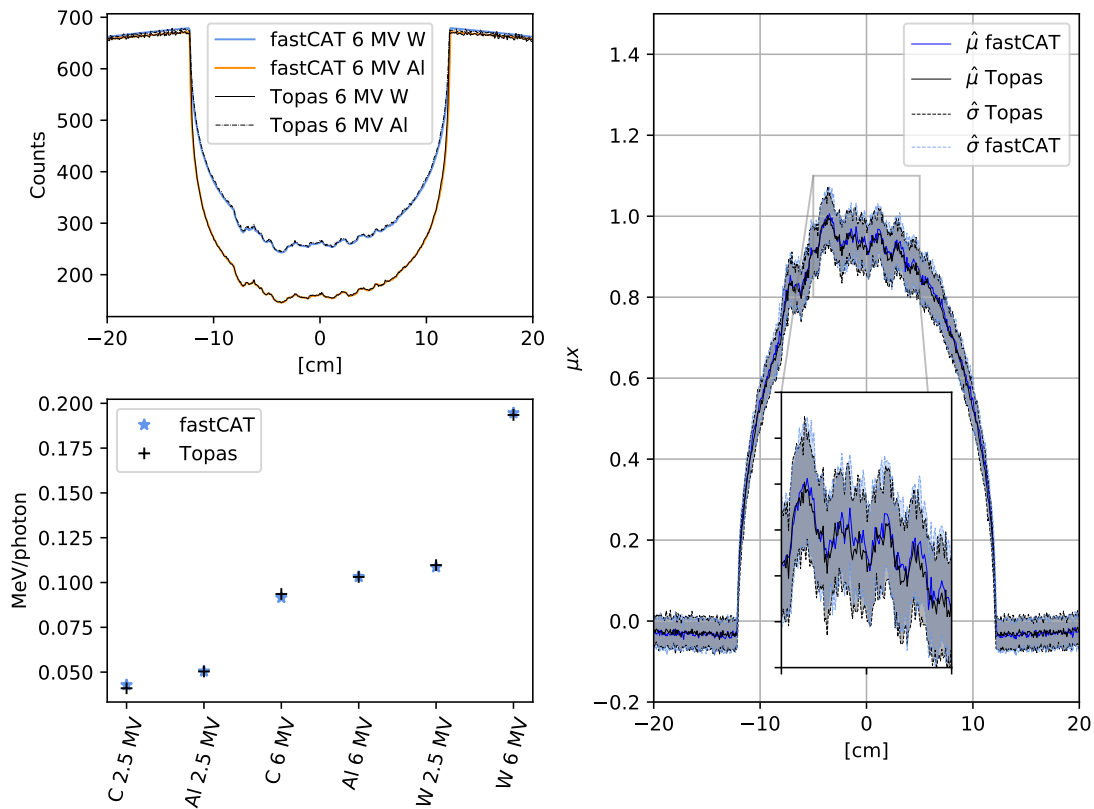


Figure 4: (Top) Scatter calculation in a Tungsten 6MV image averaged in 64 pixels in the Z direction compared to an equivalent Topas MC simulation. (Bottom) Dose comparison between fastCAT and Topas. (R) Validation of fastCAT's projection with a projection from a Topas simulation for an Aluminum target beam of 6 MV and a Tungsten target beam of 6 MV.

simulations. The projections with scatter also had good agreement with the MC values as seen in Figure 4 on the top left. With a difference of 0.21 % in the average standard deviation of all pixels between fastCAT and MC.

A demonstration of fastCAT dose calculation accuracy can be seen in Figure 4 on the bottom left. The dose showed good agreement with the MC dose estimates. Mean dose per photon in the water phantom had a difference of 1.4 % of the MC values. The largest dose estimation error was found for the Carbon 2.5 MV beam with an error of 4.5 %.

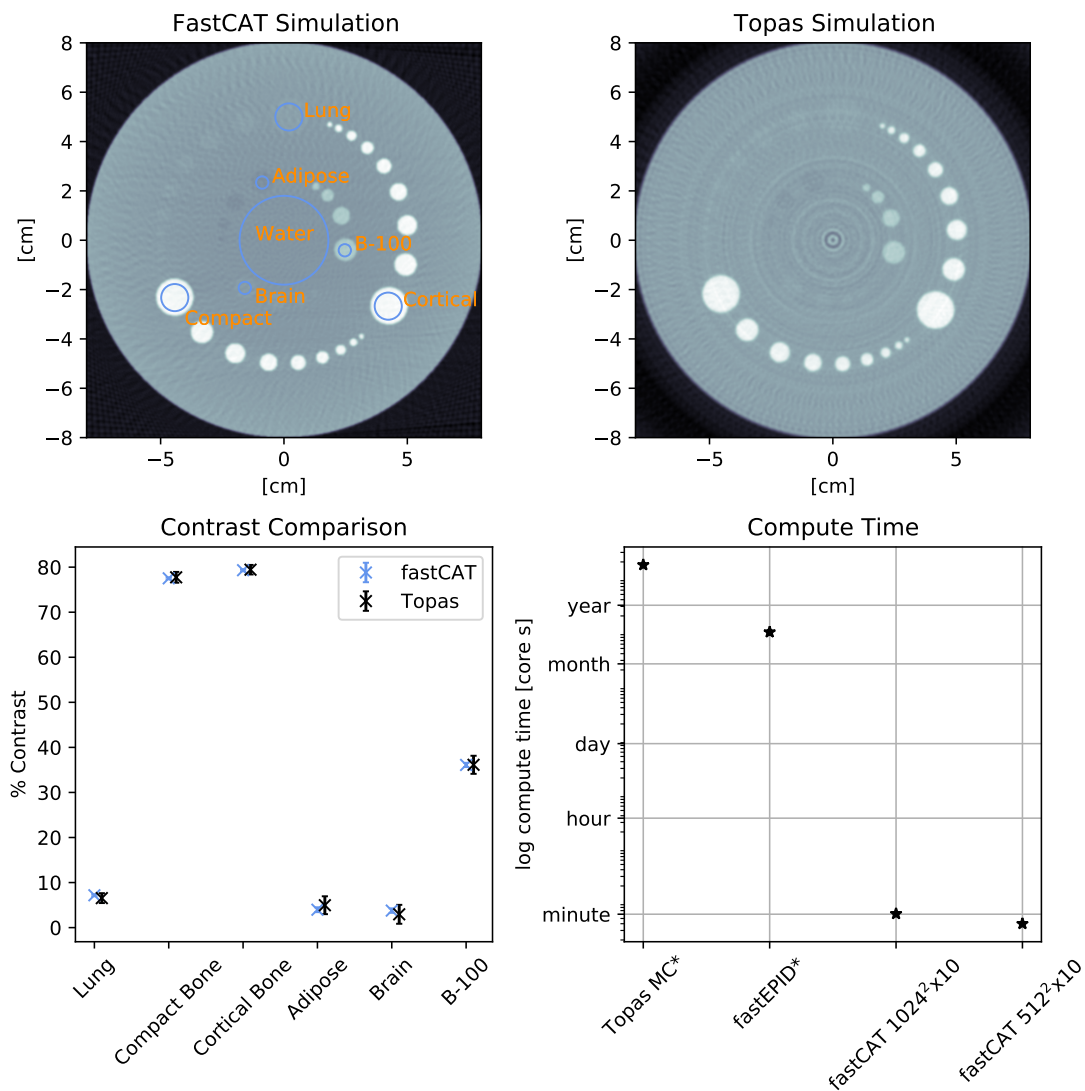


Figure 5: (Top) Results of the fastCAT simulation with the ROIs used in the contrast (L) and the Topas simulation (R). (Bottom, L) A comparison between a CBCT reconstruction in Topas and fastCAT. (Bottom, R) A logarithmic plot of the estimated simulation times for full Topas MC simulation, fastEPID, and fastCAT. *denotes extrapolated times

III.C. CBCT contrast and calculation time

This fidelity between the intensity profiles translated into excellent agreement between contrasts in a full CBCT reconstruction (Figure 5). The average difference between fastCAT and MC contrast was 0.5%. The difference for the each of the inserts was 0.6, -0.1, -0.2,

-0.9, 0.8, and 0.4 percent for the deflated lung, compact and cortical bone, adipose, brain and B-100, respectively. All differences were within the 95% confidence interval of the MC values. Streak artifact were produced due to the spatial averaging of the MC simulation along the z dimension as can be seen if Figure 5 on the top right.

A time comparison for CBCT reconstruction performed with a full Topas MC simulation, fastEPID and fastCAT for a 180-view CBCT dataset generated with 6 MV beam with a tungsten target is show in Figure 5. An extrapolation is made for a full Topas MC simulation assuming a single view with 10^9 photons takes 5.6 core years. A fastEPID simulation using the same parameters would take an estimated 0.32 core years, while the fastCAT simulations would take 40 and 61 seconds for a $512 \times 512 \times 10$ and $1024 \times 1024 \times 10$ reconstruction sizes respectively.

IV. Discussion

Overall, there was close agreement between fastCAT and MC-generated MV CBCT images. The next step will be to asses agreement between fastCAT and experimental CBCT. One validated fastCAT result is the MTF of the GOS and CWO detectors had an average error of 0.5% and 4.8% of detector measurements performed by Shi *et al.* and Star-lack respectively. This comparison lends some validity to the fastCAT simulation method. However, the full MC imaging simulations contains assumptions which may need to be modified to return result consistent with experimental data. These assumptions include; using a spatially uniform cone beam, ignoring scatter generated in the primary and secondary collimators, scoring only photons in the detector and ignoring charged particle fluence, and assuming that coherent scattering direction is not changed in the scattering event. All of these assumptions will perhaps degrade the agreement between fastCAT's results and experimental measurements. Further work will asses this fidelity and likely modify fastCAT's assumptions so as to attain the highest possible agreement with an experimental Catphan phantom.

IV.A. Limitations

FastCAT suffers from some rigidity in terms of certain parameters. For example, fastCAT uses a 16 energy approach to quantifying the detector response and scatter kernel. These

energies range from 30 keV to 6 MeV which is a good range for most MV and kV imaging applications. One notable exceptions would be mammography which often focuses on energies below 30 keV. The energy range could be modified to include these applications, however with the geometry of the simulation and the detectors discussed it was seen that photons below 30 keV rarely were detected ($>0.001\%$ of fluence).

Likewise, the detector pixel pitch is not a parameter that can be easily modified from the available built-in detectors as this requires rebinning of MC phasespace files in the case of the GOS detector. These files are too large to include in the software. For a detector like the CWO modifying the pixel pitch is even more complicated as the detector septa must be moved and the simulation rerun. The implemented scatter correction further restricts the use of fastCAT, as scatter is made for the simulation of a 16-cm diameter water phantom and the coherent scatter approximation will result in artifacts.

Additionally, in the time comparison (Figure 5 bottom right), fastCAT would suffer from memory constraints in completing simulations with high resolution reconstructions which would not be a factor in MC. Finally, large changes in SAD and SDD generate artifacts. Further work will aim to solve these rigidities.

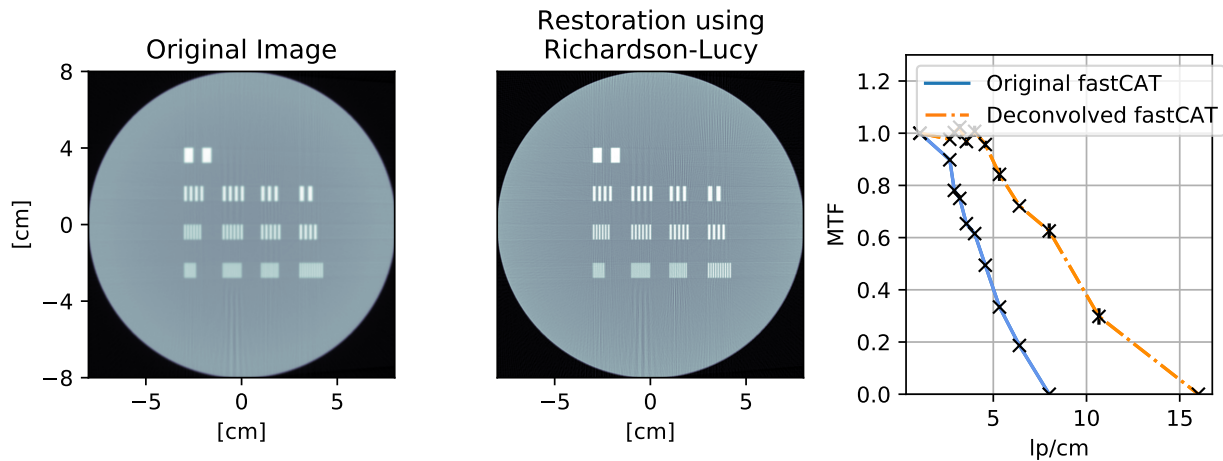


Figure 6: (L) The original fastCAT reconstruction. (Center) A deconvolution of the image using Richardson-Lucy deconvolution and the PSF from the simulation. (R) MTF for the simulation before and after deconvolution.

IV.B. Future applications

Three applications of fastCAT are speculated by the authors: Development of new CBCT methodologies (the primary goal of this platform), deconvolution of CT images using an approximation of the PSF, and dataset generation for machine learning (ML) deployment. First, fastCAT can be used to quickly assess combinations of beam energies and detector types and geometries for CBCT imaging. FastCAT greatly decreases the time it takes to simulate these combinations as it can be done in minutes while giving comparable results to MC in terms of image spatial resolution and contrast. This allows a greater flexibility in exploring the parameter space for CBCT imaging equipment and protocols. Secondly, fastCAT generates a PSF for a given beam and detector with an arbitrary focal spot size. If agreement can be achieved between the image MTF of fastCAT and a system experimental data by modification of the focal spot size, one could use the fastCAT PSF to estimate the system PSF. The knowledge of PSF allows one to perform a deconvolution of the image to improve of CBCT images. In a test case using Richardson-Lucy deconvolution^{28,29} on the fastCAT MTF phantom (Figure 6) CBCT image MTF increased by a factor of two using deconvolution of the projection images. Thirdly, fastCAT could be imagined as a tool to link simulation space to real clinical imaging. This could be done by maintaining a fastCAT model of a clinical imaging setup though adjusting user parameters available in fastCAT to agree with monthly QA images of a Catphan phantom. A clinic could then use fastCAT to generate arbitrary ML training data personalized to a given machine in terms of contrast and MTF. This overcomes some obstacles that arise in terms of ML algorithms which have to be trained on general datasets and can not necessarily respond to changes in medical imaging equipment's output over time. This allows for a more personalized approach between dataset generation that links to clinical QA. This method could provide superior performance of ML algorithms and remove risks that ML output would be invalid due to changing machine output over time. An application could be in automated segmentation of bone CBCT for patient positioning, where algorithms could be retrained on adjusted data if drift in QA MTF or contrast indicated a change in image quality.

V. Conclusion

We presented fastCAT; a fast application for MV CBCT data generation. FastCAT shows good agreement with measurements with respect to spatial resolution for a GOS and a CWO detector. The application was validated using contrast modules of a Catphan 515 and was seen to be within 1% of an equivalent monte carlo simulation for each of the brain, deflated lung, compact and cortical bone, and adipose tissues inserts respectively. The complete CBCT dataset generation for a $512 \times 512 \times 10$ and $1024 \times 1024 \times 10$ reconstruction size took 40 and 61 seconds, approximately five orders of magnitude faster than the corresponding MC simulations.

VI. Acknowledgments

The authors would like to acknowledge Chelsea Dunning for the contribution to the name fastCAT. We would also like to thank Marios Myronakis for sharing the GOS MTF data with us. The work was partly funded by an NSERC Discovery Grant and the Canada Research Chair program.

References

- ¹ A. Grzadziel, B. Smolinska, R. Rutkowski, and K. Slosarek, EPID dosimetry - Configuration and pre-treatment IMRT verification, *Reports of Practical Oncology and Radiotherapy* **12**, 307–312 (2007).
 - ² B. Mijnheer, S. Beddar, J. Izewska, and C. Reft, In vivo dosimetry in external beam radiotherapy, *Medical Physics* **40** (2013).
 - ³ S. Celi, E. Costa, C. Wessels, A. Mazal, A. Fourquet, and P. Francois, EPID based in vivo dosimetry system: clinical experience and results, *Journal of Applied Clinical Medical Physics* **17**, 262–276 (2016).
 - ⁴ P. Alaei and E. Spezi, Imaging dose from cone beam computed tomography in radiation therapy, *Physica Medica* **31**, 647–658 (2015).
-

-
- ⁵ C. Lindsay, M. Bazalova-Carter, A. Wang, D. Shedlock, M. Wu, M. Newson, L. Xing, W. Ansbacher, R. Fahrig, and J. Star-Lack, Investigation of combined kV MV CBCT imaging with a high-DQE MV detector, *Medical Physics* **46**, 563–575 (2019).
 - ⁶ M. Wu, A. Keil, D. Constantin, J. Star-Lack, L. Zhu, and R. Fahrig, Metal artifact correction for x-ray computed tomography using kV and selective MV imaging, *Medical Physics* **41** (2014).
 - ⁷ M. Myronakis, J. Star-Lack, P. Baturin, J. Rottmann, D. Morf, A. Wang, Y. H. Hu, D. Shedlock, and R. I. Berbeco, A novel multilayer MV imager computational model for component optimization:, *Medical Physics* **44**, 4213–4222 (2017).
 - ⁸ Y. H. Hu, M. Myronakis, J. Rottmann, A. Wang, D. Morf, D. Shedlock, P. Baturin, J. Star-Lack, and R. Berbeco, A novel method for quantification of beam's-eye-view tumor tracking performance, *Medical Physics* **44**, 5650–5659 (2017).
 - ⁹ S. J. Blake, P. Vial, L. Holloway, P. B. Greer, A. L. McNamara, and Z. Kuncic, Characterization of optical transport effects on EPID dosimetry using Geant4, *Medical Physics* **40**, 041708 (2013).
 - ¹⁰ M. Shi, M. Myronakis, Y.-H. Hu, M. Jacobson, M. Lehmann, R. Fueglistaller, P. Huber, P. Baturin, A. Wang, D. Ferguson, T. Harris, D. Morf, and R. Berbeco, A novel method for fast image simulation of flat panel detectors., *Physics in medicine and biology* **64**, 095019 (2019).
 - ¹¹ J. Star-Lack, M. Sun, A. Meyer, D. Morf, D. Constantin, R. Fahrig, and E. Abel, Rapid Monte Carlo simulation of detector DQE(f), *Medical Physics* **41** (2014).
 - ¹² J. Rottmann, D. Morf, R. Fueglistaller, G. Zentai, J. Star-Lack, and R. Berbeco, A novel EPID design for enhanced contrast and detective quantum efficiency, *Physics in Medicine and Biology* **61**, 6297–6306 (2016).
 - ¹³ C. Kausch, B. Schreiber, F. Kreuder, R. Schmidt, and O. Dössel, Monte carlo simulations of the imaging performance of metal plate/phosphor screens used in radiotherapy, *Medical Physics* **26**, 2113–2124 (1999).
-

-
- ¹⁴ C. Kirkby and R. Sloboda, Comprehensive Monte Carlo calculation of the point spread function for a commercial a-Si EPID, *Medical Physics* **32**, 1115–1127 (2005).
- ¹⁵ G. Hernández and F. Fernández, xpecgen: A program to calculate x-ray spectra generated in tungsten anodes, *The Journal of Open Source Software* **1**, 62 (2016).
- ¹⁶ I Kawrakow, E Mainegra-Hing, DWO Rogers, F Tessier, and BRB Walters, The EGSnrc Code System, Monte Carlo Simulation of Electron and photon Transport, NRCC Report PIRS-701, National Research Council Canada (2018).
- ¹⁷ S. Flampouri, P. M. Evans, F. Verhaegen, A. E. Nahum, E. Spezi, and M. Partridge, Optimization of accelerator target and detector for portal imaging using Monte Carlo simulation and experiment, *Physics in Medicine and Biology* **47**, 3331–3349 (2002).
- ¹⁸ D. Parsons, J. L. Robar, and D. Sawkey, A Monte Carlo investigation of low-Z target image quality generated in a linear accelerator using Varian’s VirtuaLinac, *Medical Physics* **41**, 021719 (2014).
- ¹⁹ D. Parsons and J. L. Robar, Beam generation and planar imaging at energies below 2.40 MeV with carbon and aluminum linear accelerator targets, *Medical Physics* **39**, 4568–4578 (2012).
- ²⁰ J. Baek, H. Kim, B. Kim, Y. Oh, and H. Jang, Assessment of portal image resolution improvement using an external aluminum target and polystyrene electron filter, *Radiation Oncology* **14**, 70 (2019).
- ²¹ J. Star-Lack, D. Shedlock, D. Swahn, D. Humber, A. Wang, H. Hirsh, G. Zentai, D. Sawkey, I. Kruger, M. Sun, E. Abel, G. Virshup, M. Shin, and R. Fahrig, A piecewise-focused high DQE detector for MV imaging, *Medical Physics* **42**, 5084–5099 (2015).
- ²² M. Shi, M. Myronakis, Y. H. Hu, D. Morf, J. Rottmann, and R. Berbeco, A Monte Carlo study of the impact of phosphor optical properties on EPID imaging performance, *Physics in Medicine and Biology* **63**, 165013 (2018).
- ²³ S. Agostinelli and et al., Geant4 a simulation toolkit, *Nuclear Instruments and Methods in Physics Research Section A: Accelerators, Spectrometers, Detectors and Associated Equipment* **506**, 250–303 (2003).
-

-
- ²⁴ J. Perl, J. Shin, J. Schumann, B. Faddegon, and H. Paganetti, TOPAS: An innovative proton Monte Carlo platform for research and clinical applications, *Medical Physics* **39**, 6818 (2012).
- ²⁵ M. Berger, J. Hubbell, S. Seltzer, J. Chang, J. Coursey, R. Sukumar, D. Zucker, and K. Olsen, XCOM: Photon Cross Sections Database - Version 1.5.
- ²⁶ A. Biguri, M. Dosanjh, S. Hancock, and M. Soleimani, TIGRE: A MATLAB-GPU toolbox for CBCT image reconstruction, *Biomedical Physics and Engineering Express* **2**, 055010 (2016).
- ²⁷ L. A. Feldkamp, L. C. Davis, and J. W. Kress, Practical cone-beam algorithm, *Journal of the Optical Society of America A* **1**, 612 (1984).
- ²⁸ W. H. Richardson, Bayesian-Based Iterative Method of Image Restoration*, *Journal of the Optical Society of America* **62**, 55 (1972).
- ²⁹ L. B. Lucy, An iterative technique for the rectification of observed distributions, *The Astronomical Journal* **79**, 745 (1974).
-